



# Novel Pt-carbon core–shell decorated hierarchical CoMo<sub>2</sub>S<sub>4</sub> as efficient electrocatalysts for alkaline/seawater hydrogen evolution reaction

Subramanian Vijayapradeep <sup>a</sup>, Natarajan Logeshwaran <sup>a</sup>, Shanmugam Ramakrishnan <sup>a,b</sup>, Ae Rhan Kim <sup>a</sup>, Prabhakaran Sampath <sup>d</sup>, Do Hwan Kim <sup>a,c</sup>, Dong Jin Yoo <sup>a,e,\*</sup>

<sup>a</sup> Graduate School, Department of Energy Storage/Conversion Engineering (BK21 FOUR), Hydrogen and Fuel Cell Research Center, Jeonbuk National University, 567 Baekje-daero, Deokjin-gu, Jeonju-si, Jeollabuk-do 54896, Republic of Korea

<sup>b</sup> School of Engineering, Newcastle University, Merz Court, Newcastle Upon Tyne, NE17RU, United Kingdom

<sup>c</sup> Division of Science Education and Institute of Fusion Science, Jeonbuk National University, 567 Baekje-daero, Deokjin-gu, Jeonju-si, Jeollabuk-do 54896, Republic of Korea

<sup>d</sup> Department of Nano Convergence Engineering, Jeonbuk National University, 567 Baekje-daero, Deokjin-gu, Jeonju-si, Jeollabuk-do 54896, Republic of Korea

<sup>e</sup> Department of Life Science, Jeonbuk National University, 567 Baekje-daero, Deokjin-gu, Jeonju-si, Jeollabuk-do 54896, Republic of Korea



## ARTICLE INFO

### Keywords:

Heterogeneous electrocatalyst  
Pt-C core–shell  
Hydrogen evolution reaction  
Density functional theory calculations  
Seawater electrolysis

## ABSTRACT

Electrochemical water electrolysis is a prominent method of green-hydrogen fuel production. Tailored nano-structures of Pt-based electrocatalysts have high priority in hydrogen production. Herein, we fabricated carbon-encapsulated Pt core–shell supported CoMo<sub>2</sub>S<sub>4</sub>-NGNF as an efficient electrocatalyst for the hydrogen evolution reaction (HER). The novel carbon-encapsulated Pt core shells improved the long-term durability. The Pt@CoMo<sub>2</sub>S<sub>4</sub>-NGNF hybrids displayed overpotentials of 27 mV to achieve a current density of 10 mA cm<sup>-2</sup> in 1.0 M KOH and outstanding durability of 100 h. When Pt@CoMo<sub>2</sub>S<sub>4</sub>-NGNF||IrO<sub>2</sub> was employed in overall seawater electrolysis applications, it required 1.54 V to achieve a 10 mA cm<sup>-2</sup> current density. Additionally, we evaluated the electronic structure and HER mechanism of Pt@CoMo<sub>2</sub>S<sub>4</sub> & CoMo<sub>2</sub>S<sub>4</sub> using density functional theory (DFT) calculations. This work illustrates the possibility of designing an effective, long-lasting, and scalable electrocatalyst for the electrolysis of alkaline and seawater to produce pure hydrogen.

## 1. Introduction

Exponential increases in environmental pollution and rapid energy demand require alternative sustainable, clean energy resources to control carbon footprints [1–4]. Hydrogen is one of the best green energy reservoirs in transport and large energy applications [5,6]. Water-splitting catalysis has been acknowledged as a promising potential technology to produce hydrogen in large quantities [7,8]. Water electrolysis involves two core reactions: the oxygen evolution reaction (OER) at the cathode and the hydrogen evolution reaction (HER) at the anode [9,10]. Various concerns have limited heterogeneous catalysis hydrogen production, such as sluggish reaction kinetics, inadequate catalyst optimization, and significant energy consumption in alkaline media [11,12]. Platinum (Pt)-based electrocatalysts have drawn a lot of interest for large-scale affordable pure hydrogen generation because they can be used in interface engineering and active crystalline facet

engineering [13–17]. Still, Pt is a state-of-the-art material choice in alkaline HER due to the preferred Pt-H<sub>ad</sub> formations for proficient water dissociation. Rational structural Pt-based electrocatalysts with unique enhanced catalytic activity, excellent capacity, and longer stability are of special interest [18,19]. Long-term durability issues of Pt-based heterogeneous water electrolysis can be improved by the incorporation of chemical-resistant supports. Carbon matrices such as graphene, carbon nanofibers, and fullerenes can significantly mitigate Pt nanoparticle agglomeration and improve electrical conductivity. Encapsulation of Pt nanoparticles using various carbon sources like melamine, aniline, and glucose has numerous advantages of oxidation tolerance, metal corrosion resistance, and electrical conductivity [20–23]. The thickness of the encapsulation carbon matrix would either increase or decrease the active Pt site exposure for enhanced electrical conductivity. Optimization of carbon matrix thickness is essential in unique Pt-carbon encapsulation material construction [24].

\* Corresponding author at: Graduate School, Department of Energy Storage/Conversion Engineering (BK21 FOUR), Hydrogen and Fuel Cell Research Center, Jeonbuk National University, 567 Baekje-daero, Deokjin-gu, Jeonju-si, Jeollabuk-do 54896, Republic of Korea.

E-mail address: [djyoo@jbnu.ac.kr](mailto:djyoo@jbnu.ac.kr) (D. Jin Yoo).

The combination of parallelly active Pt and earth-abundant transition metals has been proposed as an effective strategy in efficient heterogeneous water electrolysis applications [25,26]. As recently reported, Pt-supported with MoS<sub>2</sub> [27], CoO [28], MoC [29], Ti<sub>0.7</sub>Mo<sub>0.3</sub>O<sub>2</sub> [30], and CoS<sub>2</sub> [31] nanostructures displayed superior catalytic activity with enhanced durability. Strong metal–metal interactions (SMMI) [32] and interfacial/electronic interactions from combining Pt with transition metal alloys are of interest. Ternary transition metal sulfides such as Mo<sub>x</sub>S<sub>x</sub>M<sub>x</sub> (M = Co, Ni, and Fe) have excellent capacity and electrocatalytic activity with improved redox properties than binary metal sulfides due to multiple oxidation states. Molybdenum disulfide (MoS<sub>2</sub>) alone possesses comparable HER energy profiles ( $\Delta G_{H^*}$ ) and high theoretical exchange current density ( $j_0$ ) to Pt [33]. Hence, it has the promising ability of replacing Pt-based material, though limited intrinsic active sites and electrical conducting properties make its utility doubtful. Efforts such as defect engineering, structural optimization, and regulating metal composition have been made to increase active site exposures. Cobalt (Co) elemental doping is a promising choice to provide additional active sites and enhance the overall HER performance [34,35]. Co-Mo-S doping can also influence the charge carrier density in MoS<sub>2</sub>. The presence of Co dopants alters the balance between electrons and holes in the material, leading to a higher concentration of either carriers depending on the specific doping conditions. This modulation of carrier density can further enhance the electrical conductivity of Co-Mo-S compared to undoped MoS<sub>2</sub> [36,37]. Even an additional carbon matrix-assisted Co-Mo-S would provide multiple advantages for practical HER applications [38].

Herein, we fabricated carbon-encapsulated Pt-carbon core–shell deposited on self-supported CoMo<sub>2</sub>S<sub>4</sub> hierarchically grown N-doped graphene nanofibers (Pt-C@CoMo<sub>2</sub>S<sub>4</sub>-NGNF) as efficient and scalable electrocatalysts for HER in alkaline and seawater media. Initially, typical CoMo<sub>2</sub>S<sub>4</sub> nanosheets were hierarchically grown on uniform N-doped conducting GNF using a facile hydrothermal technique. Then, Pt-carbon core shells were separately developed using a Pt-aniline complex in a simple thermal reduction method. Specific ratios of aniline complex and Pt ions were maintained to deliver the optimal carbon layer thickness-coated shell formation on Pt nanoparticles. Then, typically prepared CoMo<sub>2</sub>S<sub>4</sub>-NGNF and Pt-aniline complexes were sintered under an inert environment. The obtained Pt-C@CoMo<sub>2</sub>S<sub>4</sub>-NGNF hybrid electrocatalysts with ternary transition metal sulfides resulted in effective activities of Pt, while N-atoms interacted with various carbon matrix supports. This can facilitate SMMI and electronic/interfacial heterojunction interactions to help tune the adsorption activity and electron delocalization capacity. Due to the previously mentioned physico-chemical features, fabricated Pt-C@CoMo<sub>2</sub>S<sub>4</sub>-NGNF hybrids showed overpotentials of 27 mV and 79 mV to obtain an HER current density of 10 mA cm<sup>-2</sup> and 100 mA cm<sup>-2</sup>, respectively, in 1.0 M KOH. Prominently, Pt-C@CoMo<sub>2</sub>S<sub>4</sub>-NGNF delivers high stability and retains ~ 95% operating current density after a 100 h durability test. We carried Pt-C@CoMo<sub>2</sub>S<sub>4</sub>-NGNF||IrO<sub>2</sub> as cathodic and anodic electrodes in the overall water electrolysis system. The system required 1.52 V to obtain a current density of 10 mA cm<sup>-2</sup> in 1.0 M KOH solution. This novel Pt-C@CoMo<sub>2</sub>S<sub>4</sub>-NGNF hybrid significantly increased catalytic activity and long-term durability compared to Pt-C. Additionally, we evaluated HER activities of Pt-C@CoMo<sub>2</sub>S<sub>4</sub>-NGNF in an alkaline seawater medium, which displayed an overpotential of 1.54 V and 1.67 V to obtain respective current densities of 10 mA cm<sup>-2</sup> and 200 mA cm<sup>-2</sup>. We also studied the adsorption energy profiles of Pt@CoMo<sub>2</sub>S<sub>4</sub>, CoMo<sub>2</sub>S<sub>4</sub>, and Pt using first-principle density functional theory calculations. As a proof of concept, these findings demonstrate the unusual HER activity of Pt-C@CoMo<sub>2</sub>S<sub>4</sub>-NGNF hybrids in both alkaline and seawater conditions.

## 2. Experimental section

### 2.1. Synthesis of CoMo<sub>2</sub>S<sub>4</sub>@NGNF

Raw commercial GNFs powder was immersed in 13.0 M HNO<sub>3</sub> for 48 h to remove the metal impurities, which were then filtered out. The resulting product was washed with deionized water (DI)/ethanol until it reached a neutral pH condition. A typical CoMo<sub>2</sub>S<sub>4</sub>@NGNF hierarchical structure was prepared using a facile hydrothermal method. Briefly, nitrogen-functionalized graphene nanofiber (NGNF) powder was dispersed in 15 mL of deionized water and ultrasonicated for 2 h at room temperature. Then, 0.1:0.2:0.4 mmol ratio of Co(NO<sub>3</sub>)<sub>2</sub>·6H<sub>2</sub>O: Na<sub>2</sub>MoO<sub>4</sub>·2H<sub>2</sub>O: C<sub>2</sub>H<sub>5</sub>NS precursors was dissolved in 5 mL of DI water separately with mechanical stirring for 1 h. The above solutions were added dropwise to the GNF solution under controlled magnetic stirring conditions. Then, the final mixture was transferred into a 100 mL Teflon autoclave vessel and was maintained at a heating temperature of 200 °C for 12 h. The resulting product was washed several times with DI water and ethanol. The obtained product was then dried overnight at 60 °C in a vacuum oven.

### 2.2. Synthesis of Pt-C@CoMo<sub>2</sub>S<sub>4</sub>-NGNF

The Pt-aniline complex was prepared by placing 0.12 g of H<sub>2</sub>PtCl<sub>6</sub>·6H<sub>2</sub>O in 35 mL of aniline with stirring for 6 h at room temperature. Then, the mixture was filtered using 0.2 M HCl in a rotary vacuum pump to remove the excess unreacted aniline and dry it in a vacuum oven at 60 °C to obtain the dark purple color of the Pt-aniline complex. Then, typically obtained CoMo<sub>2</sub>S<sub>4</sub>-NGNF and Pt-aniline complex was dissolved in 50 mL of ethanol and stirred for 30 min. The rotary vacuum pump was employed to evaporate the ethanol solution. Finally, the resulting Pt-aniline complex-coated CoMo<sub>2</sub>S<sub>4</sub>-NGNF was sintered in a tubular furnace at 500 °C under an inert N<sub>2</sub> atmosphere for 1 h.

## 3. Results and discussion

### 3.1. Morphological and structural investigations of CoMo<sub>2</sub>S<sub>4</sub>-NGNF/Pt-C@CoMo<sub>2</sub>S<sub>4</sub>-NGNF nanohybrids

The synthesis procedures of CoMo<sub>2</sub>S<sub>4</sub>-NGNF and Pt-carbon core–shell on CoMo<sub>2</sub>S<sub>4</sub>-NGNF are illustrated in Fig. 1. Pt-carbon nanoparticle encapsulation on the CoMo<sub>2</sub>S<sub>4</sub>@NGNF nanohybrids was achieved by a facile, cost-effective, single-step in-situ hydrothermal and calcination process. A strong bond between a metal–metal formation with carbon results in high synergistic interactions of CoMo precursors and graphene nanofiber (GNF). The ability of the carbon matrix to act as an electron mediator to transfer electrons from the catalyst surface to the H<sub>2</sub> evolution is a fascinating function of GNFs [39]. During the hydrothermal reaction, the generated H<sub>2</sub>S gas effectively converted metal oxides into their corresponding sulfides. Also, the released NH<sub>3</sub> gas effectively doped nitrogen into the graphene nanofiber skeleton [40], which ensures the formation of flower-like CoMo<sub>2</sub>S<sub>4</sub> on GNF during the hydrothermal reactions. In the subsequent thermal reduction process of Pt-carbon core–shell formation, aniline complexes provide nitrogen for the carbon sources. During the inert (N<sub>2</sub>) environment graphitization, sintering process, carbon skeletons from aniline provide additional nitrogen supports on individual Pt particles as well as the CoMo<sub>2</sub>S<sub>4</sub>-NGNF surfaces. This intrinsic synergy of N atom doping can influence the durability, capability of Pt-C@CoMo<sub>2</sub>S<sub>4</sub>-NGNF (PC@CMS-NG) nanohybrids and their HER performances. Morphological and structural investigations of prepared electrocatalysts were evaluated using field emission scanning electron microscopy (FE-SEM) and high-resolution transmission electron microscopy (HR-TEM). Fig. 2a represents FE-SEM images of CoMo<sub>2</sub>S<sub>4</sub>-NGNF (CMS-NG) nanohybrids, which exhibit consistent growth of hierarchical CoMo<sub>2</sub>S<sub>4</sub> nano petals on the skeleton of N-doped carbon nanofiber. The high-resolution elemental color

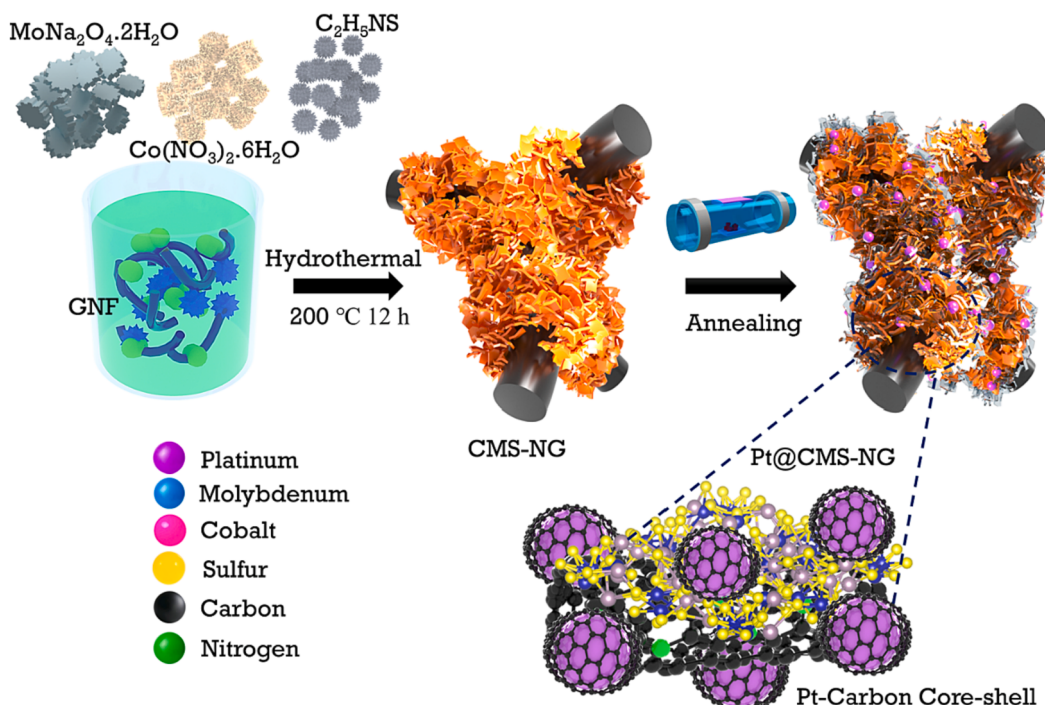


**Fig. 1.** Schematic illustration of the synthetic process of CoMoS on N-doped GNF using a facile hydrothermal method followed by inert annealing to develop PC@CMS-NG.

mapping in Fig. S1 (supporting information) confirmed the existence of elements Mo, Co, S, N, C, and environmental O in CMS-NG nanohybrids. Also, additional morphology supports of CoMo<sub>2</sub>S<sub>4</sub>-NGNF are included in Fig. S1. Spherical aberration-corrected scanning transmission electron microscope (CS-TEM) images in Fig. 2b confirmed the uniform size of CMS growth optimized through the thiourea-assisted hydrothermal process. Fig. 2c shows respective HR-TEM images in which calculated lattice fringe distances of 0.27, 0.29, 0.33, and 0.35 correspond to (311), (-402), (-311), and (-113) planes of CoMo<sub>2</sub>S<sub>4</sub>. Fig. S2(a-d) shows the respective lattice fringes calculation evidence of CMS-NG. It is important to note that thiourea can act as dual precursors of sulfur and nitrogen during the hydrothermal process to achieve CoMo<sub>2</sub>S<sub>4</sub>-NGNF nanohybrids. This morphology study of CMS-NG supports the successful uniform growth of CoMo<sub>2</sub>S<sub>4</sub> hierarchical nano petals on N-doped GNF skeletons. The FE-SEM results in Fig. 2d demonstrate the formation of carbon core-shells and effective Pt-C core-shell incorporation on CMS-NG surfaces. Both the hierarchical CMS nano petals and N-doped GNF surfaces were uniformly covered with Pt-carbon core shells. Compared with the CMS-NG FE-SEM results (Fig. 2a and d), the roughness and surface morphology of PC@CMS-NG were drastically increased. Further insights corresponding to CS-TEM analysis are displayed in Fig. 2e. This clearly shows the uniform amount of Pt-C core-shell wrapping on the surface of CMS-NG. This can induce numerous Pt-H<sub>ad</sub> active sites and mobilize electron transport capability for better HER performance. Fig. 2f HR-TEM images of respective PC@CMS-NG show that the atomic-level Pt nanoparticles were uniformly covered on CMS-NG carbon supports. Individual histogram calculation results in Fig. S3a show that the average particle size distributions of Pt nanoparticles (with an average particle size of ~4 nm) are primarily developed on the active sites of CMS-NG surfaces. An additional interplanar distance calculation of Pt (111) plane about 0.23 nm and its atomic-scale STEM images in Fig. S3b show effective Pt particle deposition. High-resolution elemental color mapping results of PC@CMS-NG in Fig. 2g strongly support the existence of Pt, Co, Mo, S, N, and C elements in the PC@CMS-NG nanohybrids. Micro-Raman analysis is an ideal tool to investigate defects in graphitic carbon materials corresponding to the

E<sub>2g</sub> stretching vibration mode of sp<sup>2</sup> hybridized carbon atoms [41]. After Pt nanoparticles were coated on the CoMo<sub>2</sub>S<sub>4</sub>-NGNF, G band position moved to 1587 cm<sup>-1</sup> from CMS-NG (1585 cm<sup>-1</sup>), demonstrating strong interactions between ultrafine Pt nanoparticles and CMS-NG in Fig. 3a. The D and G intensity ratios (I<sub>D</sub>/I<sub>G</sub>) for PC@CMS-NG, CMS-NG, and GNF were 1.29, 1.10, and 1.09, respectively. The pristine GNF showed increased G band intensity with a lower intensity ratio of I<sub>D</sub>/I<sub>G</sub> compared to CMS-NG. Peaks around 618 cm<sup>-1</sup> and 924 cm<sup>-1</sup> were derived from strong metal chalcogens (CoMo<sub>2</sub>S<sub>4</sub>). Further, the increased I<sub>D</sub>/I<sub>G</sub> value after deposition of Pt-C nanoparticles on CoMo<sub>2</sub>S<sub>4</sub>-NGNF using the annealing method confirmed the successful formation of Pt-C on CoMo<sub>2</sub>S<sub>4</sub>-NGNF. Furthermore, X-ray pattern (XRD) was carried out to evaluate the phase structure of the as prepared electrocatalysts. Fig. 3b shows the XRD spectra of GNF, CMS-NG, and PC@CMS-NG nanohybrids. The broad peak around 26.5° in GNF is the (002) plane of the carbon skeleton. This formed after the successful concentrated acidification process of GNF, which eliminated unreacted metal and inorganic substances. Detailed product preparation procedures can be found in the experimental section. During hydrothermal treatment, a combination of cobalt, molybdenum precursor, and thiourea was utilized to react with GNF, leading to the growth of flower-like CoMo<sub>2</sub>S<sub>4</sub> on N-doping GNF. The corresponding peaks of CoMo<sub>2</sub>S<sub>4</sub> were found around 27.3°, 33.5°, 37.6°, 41.9°, 47.6°, and 56.1° belonging to (202), (400), (312), (024), (006) and (040) planes, respectively. These XRD peaks are consistent with the standard pattern of CoMo<sub>2</sub>S<sub>4</sub> (JCPDS card No: 01-071-0378), and the intensity of the (002) plane GNF is comparatively reduced due to effective formation of CMS during the hydrothermal method. These results strongly support the HR-TEM interplanar calculations of CMS-NG. After the Pt decoration using the carbonization process, the peaks around 39.8°, 46.3°, 67.7°, and 81.5° are related to (111), (200), (220), and (311) planes of cubic Pt. This strongly suggests the successful formation of active Pt nanoparticles over the CMS-NG surfaces. These planes are perfectly matched with the standard XRD pattern of the (JCPDS card No: 01-87-0640) for cubic Pt. The observed decrease in CoMo<sub>2</sub>S<sub>4</sub> metal peaks in PC@CMS-NG can be attributed to stacking faults [42], which occur due to irregularities in the

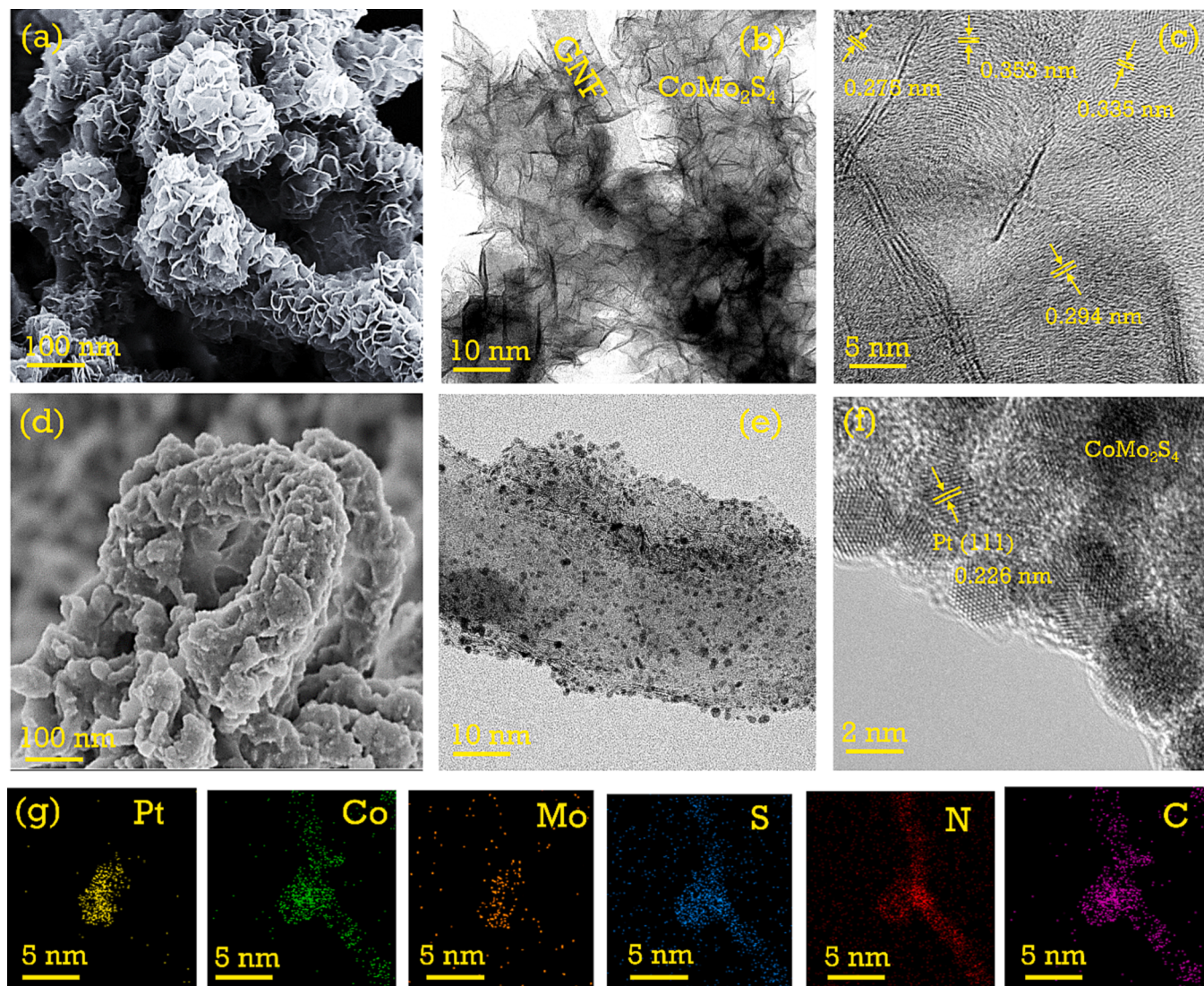


**Fig. 2.** Material morphology studies: (a) FE-SEM, (b) CS-TEM, and (c) HR-TEM images of CMS-NG. (d) FE-SEM, (e) CS-TEM, and (f) HR-TEM images of PC@CMS-NG. (g) Respective elemental color maps of Pt, Co, Mo, S, N, and C elements in the PC@CMS-NG hybrid.

arrangement of atoms within the crystal lattice, causing disruptions in the periodic stacking of crystal planes. Also, higher intensity of Pt XRD pattern overshadows the clear visibility of  $\text{CoMo}_2\text{S}_4$  peaks in PC@CMS-NG. These Pt active site-wrapped CMS-NG surfaces might enhance electron-transport kinetics to improve the overall HER performances. The Brunauer-Emmett-Teller (BET) technique has been extensively used to analyze the surface areas of the prepared materials by the semi-empirical fitting of gaseous product adsorption isotherms. Fig. S4 shows the measured nitrogen adsorption isotherm curves in which CMS-NG and PC@CMS-NG nanohybrids exhibit specific surface areas of  $78 \text{ m}^2 \text{ g}^{-1}$  and  $96 \text{ m}^2 \text{ g}^{-1}$ , respectively. This suggests that the inert environment carbonization process of PC@CMS-NG nanohybrids highly influences the materials porous nature. Additionally, corresponding Barret-Joyner-Halenda model (BJH) curves were supplied in inside Fig. S4. CMS-NG and PC@CMS-NG show the pore-size distributions of 9.2 and 19.6 nm. PC@CMS-NG nanohybrids can significantly improve mass transportation kinetics to achieve better HER performance due to their highly mesoporous nature and high specific surface nature. Thermal stability and relative composition of the prepared electrocatalyst materials were evaluated through thermogravimetric analysis (TGA). Fig. S5 shows the oxygen atmospheric TGA profiles of GNF, Pt-C, CMS-NG, and PC@CMS-NG where the residue values were  $5.97 < 18.01 <$

$38.67 < 41.77\%$ . This demonstrates the metallic thermal stability in high-temperature conditions.

The elemental valence states and surface compositions of CMS-NG and PC@CMS-NG nanohybrids were evaluated using X-ray photoelectron spectroscopy (XPS). Fig. S6a depicts the XPS survey spectrum of CMS-NG and PC@CMS-NG electrocatalysts to identify the existence of Co, Mo, S, C, N and Pt, Co, Mo, S, C, N elements respectively. Pt 4f high-resolution XPS spectra in Fig. 3c were deconvoluted into two significant components for each spin-orbit state of Pt  $4f_{5/2}$  and Pt  $4f_{7/2}$  with a binding energy difference of  $\sim 3.43 \text{ eV}$ . In which their  $\text{Pt}^0$  and  $\text{Pt}^{2+}$  states were deconvoluted as (74.8, 71.3 eV) and (75.7, 72.1 eV) respectively.

Further comparative Mo 3d high-resolution XPS deconvolution spectra for CMS-NG and PC@CMS-NG nanohybrids were supplied in Fig. 3d. The Mo  $3d_{5/2}$  binding energies of  $\text{Mo}^{4+}$ ,  $\text{Mo}^{5+}$ , and  $\text{Mo}^{6+}$  states were observed at 228.8, 230.7, and 231.9 eV respectively, while the Mo  $3d_{3/2}$  binding energies of  $\text{Mo}^{4+}$ ,  $\text{Mo}^{5+}$ , and  $\text{Mo}^{6+}$  states were 232.7, 234.2, and 235.6 eV for CMS-NG. After Pt-C core-shell incorporation, there was a slight negative shift of  $\sim 0.55 \text{ eV}$  in Mo  $3d_{5/2}$  ( $\text{Mo}^{4+}$ ,  $\text{Mo}^{6+}$ ) at 228.8, 231.8 eV and Mo  $3d_{3/2}$  ( $\text{Mo}^{4+}$ ,  $\text{Mo}^{6+}$ ) at 232.6, 235.4 eV were observed compare with bare CMS-NG. It suggests the successful metallic Pt formation in the PC@CMS-NG nanohybrids. Noticeably after the Pt-C core-shell existence Mo  $3d_{5/2}$  peaks were significantly suppressed [43],

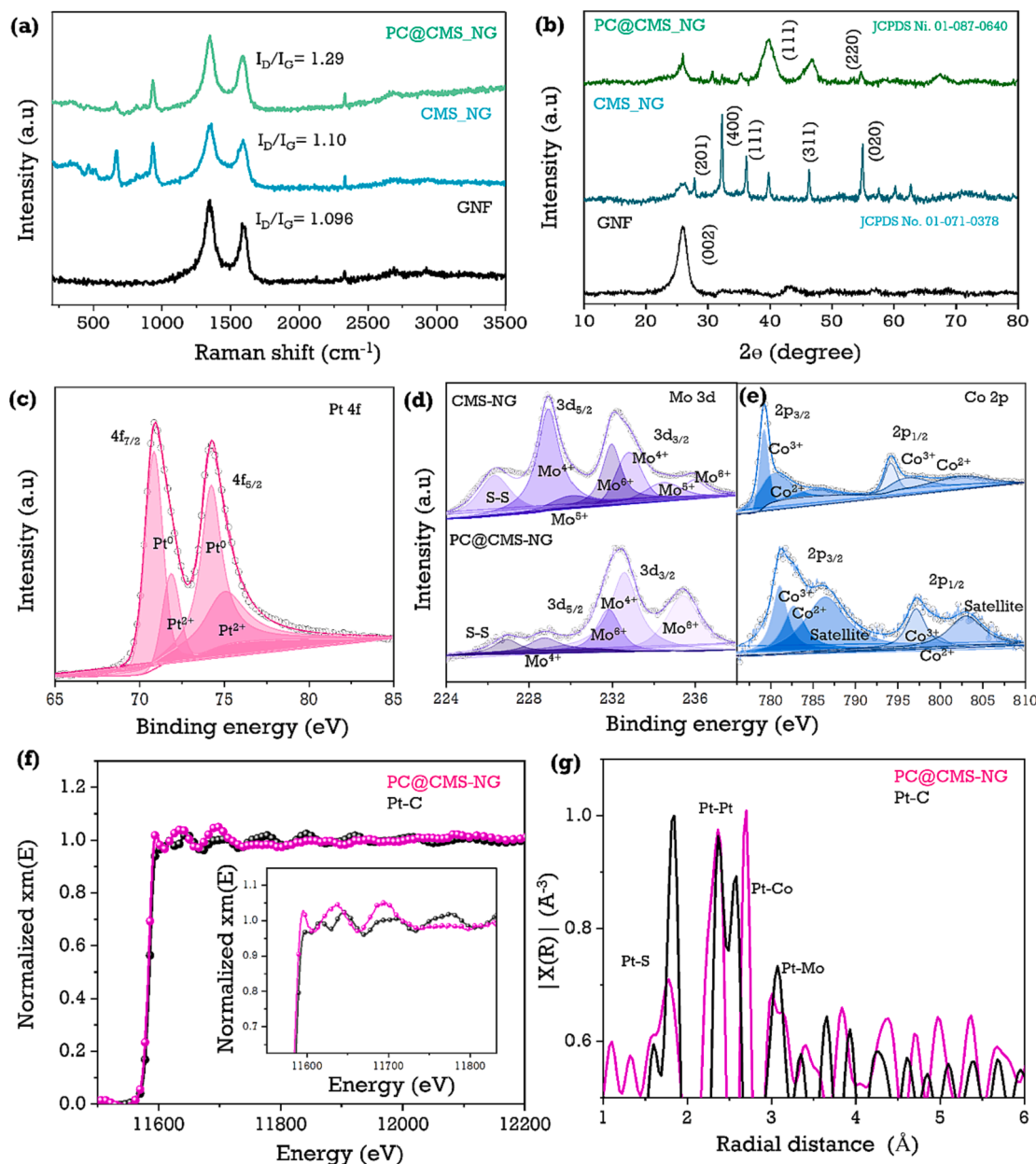


**Fig. 3.** Physiochemistry surface morphology study: (a) high-resolution Raman spectrum, (b) powder XRD spectrum of PC@CMS-NG, CMS-NG, and GNF. High-resolution XPS spectra of PC@CMS-NG element (c) Pt 4f, and compared to CMS-NG, PC@CMS-NG (d) Mo 3d, (e) Co 2p, (f) Pt-L<sub>3</sub> edge XANES spectra, and (g) FT-EXAFS spectra of PC@CMS-NG.

and due to electronic modulation supports, temperature and surface oxidation effects simultaneous modified Mo 3d<sub>3/2</sub> peaks were observed [44]. Similarly, the high-resolution comparative Co 2p XPS deconvolution spectra for CMS-NG and PC@CMS-NG nanohybrids were depicted in Fig. 3e. In which Co 2p<sub>3/2</sub> deconvoluted into respective Co<sup>3+</sup> and Co<sup>2+</sup> states at 779.0, 780.67 eV, corresponding Co 2p<sub>1/2</sub> (Co<sup>3+</sup>/Co<sup>2+</sup>) states deconvoluted into at (794.3/796.2 eV) respectively. After the Pt-C core–shell incorporation, there were significant changes observed in Co 2p<sub>3/2</sub> deconvolution such as Co<sup>3+</sup> and Co<sup>2+</sup> has shifted to 781.5 and 783.7 eV. For Co 2p<sub>1/2</sub> it shifted to 794.6, 796.5 eV respectively. This distinctive metallic characteristic of cobalt has the potential to induce d-band center delocalization within CoMo<sub>2</sub>S<sub>4</sub> composite, thereby it could enhance the overall electrical conductivity nature. Additionally, the S 2p XPS spectra of CMS-NG and PC@CMS-NG were deconvoluted and compared the two major S 2p<sub>3/2</sub> and S 2p<sub>1/2</sub> peaks. There was a slight peak shift that appeared in S 2p<sub>3/2</sub> around 161.7 and 161.9 eV, as the

peaks of S 2p<sub>1/2</sub> were observed at 163.1 and 163.3 eV. In addition, the oxidized sulfur peak around 169.2 eV was removed in PC@CMS-NG nanohybrids due to the effective inert carbonization process (Fig. S6 d). To the clear understanding of elemental peak position comparison in CMS-NG & PC@CMS-NG we have provided Table S1 in the supporting information (SI). These results evident the successive Pt-carbon incorporation on the CoMo<sub>2</sub>S<sub>4</sub>-NGNF surfaces. In which effective electronic modulation, delocalization of d-band center alteration in the Co-Mo interfaces could increase the electron charge transfer property between the Pt/Co-Mo metal–metal interactions [45]. This interfacial/electronic interactions from combining Pt with transition metal alloys possess efficient water dissociation process. The core level C 1s XPS spectra and N 1s XPS spectra were deconvoluted, and a detailed explanation is available in the supporting information. We mainly used X-ray absorption fine spectroscopy (XAFS) for the Pt elements to understand the electronic states and configuration properties of the CMS-NG after

the Pt-C core–shell incorporation. Fig. 3f shows the normalized X-ray absorption near-edge structure (XANES) spectra of the Pt L<sub>3</sub>-edge of PC@CMS-NG with references to Pt-foil. The inset image of Fig. 3f supports the uniform dispersion of Pt-C core–shell in the mixtures of Pt<sup>2+</sup> and metallic Pt<sup>0</sup> valence states. This is also evident in the XPS deconvolution spectra of Pt 4f. This high metallic Pt concentration might increase the hydrogen evolution capability of PC@CMS-NG nanohybrids. The Fourier-transformed extended X-ray absorption fine structure (EXAFS) of PC@CMS-NG and Pt-foil in Fig. 3g shows the electronic coordination of Pt with neighboring elements. The shoulder peaks around 2.4–3.5 Å belong to metal–metal Pt-Pt, Pt-Mo, and Pt-Co interactions. Peaks around 1.75–2.2 Å belong to the Pt-S and Pt-atmospheric oxygen interactions. Respective Pt K-edge EXAFS oscillation frequencies of PC@CMS-NG in k space (k<sup>2</sup>-weighting) are given in Fig. S7 (Supporting information). The metal quantity of the PC@CMS-NG was further investigated by the ICP-OES method. The obtained result confirmed that the loadings of Pt, Mo, and Co were 9.3, 4.1, and 5.3% (Table S2), respectively.

### 3.2. Electrochemical evaluations of CoMo<sub>2</sub>S<sub>4</sub>-NGNF and Pt-C@CoMo<sub>2</sub>S<sub>4</sub>-NGNF for HER

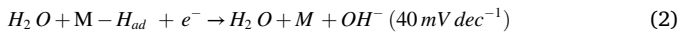
The HER electrochemical responses of typically prepared CMS-NG and PC@CMS-NG were measured in alkaline and alkaline seawater environments using traditional cyclic voltammetry (CV), linear sweep voltammetry (LSV), electrical impedance spectroscopy (EIS), and chronopotentiometry techniques. Fig. 4a depicts the schematic three-electrode setup of PC@CMS-NG HER in a 1.0 M KOH electrolyte environment. The detailed electrochemical setup is described in the electrochemical evaluation and characterization part in the supporting information. The capacitance and ohmic resistance-revised iR-corrected polarization curves of linear sweep voltammetry (LSV) in Fig. 4b demonstrate that the optimized PC@CMS-NG, commercial Pt-C, CMS-NG, and GNF catalysts exhibit minimal onset potentials and only requires iR-corrected overpotential ( $\eta$ ) of 27 mV, 36 mV, 246 mV, and 455 mV, respectively. These measurements were obtained using a constant scan rate of 1 mV s<sup>-1</sup> at a standard current density of 10 mA cm<sup>-2</sup>. In addition, to achieve current densities of 100, 200, and 250 mA cm<sup>-2</sup>, the PC@CMS-NG nanohybrids only require  $\eta$  values of 79 mV, 119 mV, and 140 mV, respectively. Due to the highly active Pt-C core shells exposed on the active edge of CoMo<sub>2</sub>S<sub>4</sub> surfaces, the conducting carbon skeletons facilitate a high electron transfer phenomenon from the metal surfaces. Respective Tafel plots in Fig. 4c show that PC@CMS-NG nanohybrids possess a relatively smaller Tafel slope value of 32 mV dec<sup>-1</sup> in comparison with that of CMS-NG, GNF, and Pt-C Tafel slope value of 88 mV dec<sup>-1</sup>, 153 mV dec<sup>-1</sup>, and 47 mV dec<sup>-1</sup>. This verifies the rapid HER catalytic reaction kinetics of PC@CMS-NG nanohybrids.

The HER reaction rates mainly depend on three essential reactions, and the steps are as follows.

Volmer reaction:



Heyrovsky reaction:



Tafel reaction:



Here, M = Metals (Pt, Mo, Co) is material surface-unoccupied sites for H<sup>+</sup> adsorption. The above three reactions might be used to calculate the total rate of HER catalysis. The entire HER went through three elementary states: the beginning state (H<sup>+</sup>), the adsorbed intermediate state (H<sup>\*</sup>), and the terminal product (1/2 H<sub>2</sub>). The derived Tafel slope of PC@CMS-NG nanohybrids suggests that the Volmer-Heyrovsky reaction of molecular H<sub>2</sub> formation could follow all HER catalysis reactions. In

the PC@CMS-NG, Pt-C core–shell active sites combined with highly conductive CMS-NG can facilitate robust contact between electrolyte and electrode surfaces to facilitate high charge transfer. This is apparent from the electrochemical impedance spectroscopy (EIS) results of charge transfer resistance (R<sub>ct</sub> = 1.17 Ω), which was significantly lower than that of CMS-NG (1.89 Ω), GNF (2.4 Ω), and commercial Pt-C (1.35 Ω) as shown in Fig. S8(a-d). This confirms the excellent ion/electron transportation in PC@CMS-NG nanohybrids compared to other prepared catalysts. We further calculated the Turnover frequency (TOF) of PC@CMS-NG to identify the intrinsic catalytic active sites for HER activity. This presents a TOF value of about 0.218 s<sup>-1</sup>, which is higher than the 0.0014 s<sup>-1</sup> of CMS-NG TOF at an overpotential of 133 mV. The origin of improved HER activity is evaluated from the electrochemical active surface area (ECSA) by CV curves recorded at various scan rates in the non-faradaic region to estimate the electrochemical double layer capacitance (C<sub>dl</sub>) of the prepared electrocatalysts. In Fig. S9(a-h) and Fig. S10, the calculated C<sub>dl</sub> values of porous PC@CMS-NG, Pt-C, CMS-NG, and GNF are 32.17 mF cm<sup>-2</sup>, 31.03 mF cm<sup>-2</sup>, 24.02 mF cm<sup>-2</sup>, and 12.50 mF cm<sup>-2</sup>, respectively. This result demonstrates the improved active surface area and increased active sites through the porous nature of Pt-C core–shell nanoparticles developed on the CMS-NG, which offers numerous catalytic active sites and vigorous OH<sup>-</sup> adsorption properties. Fig. S11(a-b) shows calculated contact angles for PC@CMS-NG, Pt-C CMS-NG, and GNF, bare carbon paper of 81.5°, 81.6°, 118.89°, 138.93°, and 66.06° respectively, in 1.0 M KOH. This confirmed that the hydrophilic nature of PC@CMS-NG enhanced the catalyst surface electron movement in overall water splitting. Hence, this rational design of PC@CMS-NG electrocatalysts offers proficient charge transfer and large porous surface areas, which could improve HER activity. Fig. 4d and Fig. S12a show the before and after LSV responses of 5000 HER CV cycles using PC@CMS-NG nanohybrids. Minute potential differences of 0.03 V and 0.037 V were observed at 100 and 200 mA cm<sup>-2</sup> current densities, respectively. The prolonged durability and stability of PC@CMS-NG nanohybrids toward HER were evaluated by the chronopotentiometry test. Fig. 4e displays the PC@CMS-NG chronopotentiometry profiles of 10 mA cm<sup>-2</sup>, 50 mA cm<sup>-2</sup>, and 100 mA cm<sup>-2</sup> applied current densities over 100 h of duration. This suggests that the material has commercial characteristics due to its high stability at high current densities. A multi-step chronopotentiometry test was also carried out for PC@CMS-NG at 10 to 50 mA cm<sup>-2</sup> with a constant time interval for 10000 s duration, as shown in Fig. S12b. Additional detailed explanations of stability studies and multi-potential studies are explained in the supporting information. These results revealed no significant potential difference, indicating that PC@CMS-NG electrodes have good durability, enhanced conductivity, superior mass transport, and mechanical properties. Comparison studies of PC@CMS-NG for HER performances with recently published electrocatalyst materials are listed in Fig. 4f and Table S3. Furthermore, we investigated morphological changes and chemical composition variations after the long-term durability test using SEM and XPS analysis as shown in Fig. S13, S14. The detailed findings are discussed in the supporting information. Overall, our results demonstrate that Pt-C@CoMo<sub>2</sub>S<sub>4</sub>-NGNF has a superior electrocatalytic activity for efficient HER performance.

### 3.3. Theoretical analysis and results

Inspired by the above HER performances of PC@CMS-NG electrocatalysts, the electronic configurations and interfacial/electronic interactions from combining Pt metal with transition metal alloys were evaluated from the density functional theory (DFT) calculations in alkaline conditions. The optimization of CoS, MoS, CoMoS, and Pt-CoMoS projections are provided in the supporting information in Fig. S15-S17. The proposed projected electronic configuration of Pt metal atoms with CoMo<sub>2</sub>S<sub>4</sub> surfaces is shown in Fig. 5a. To better understand the cause of rapid charge transfer and the Pt-CoMo<sub>2</sub>S<sub>4</sub> layer's affinity for intermediates, density of states (DOS) evaluations was

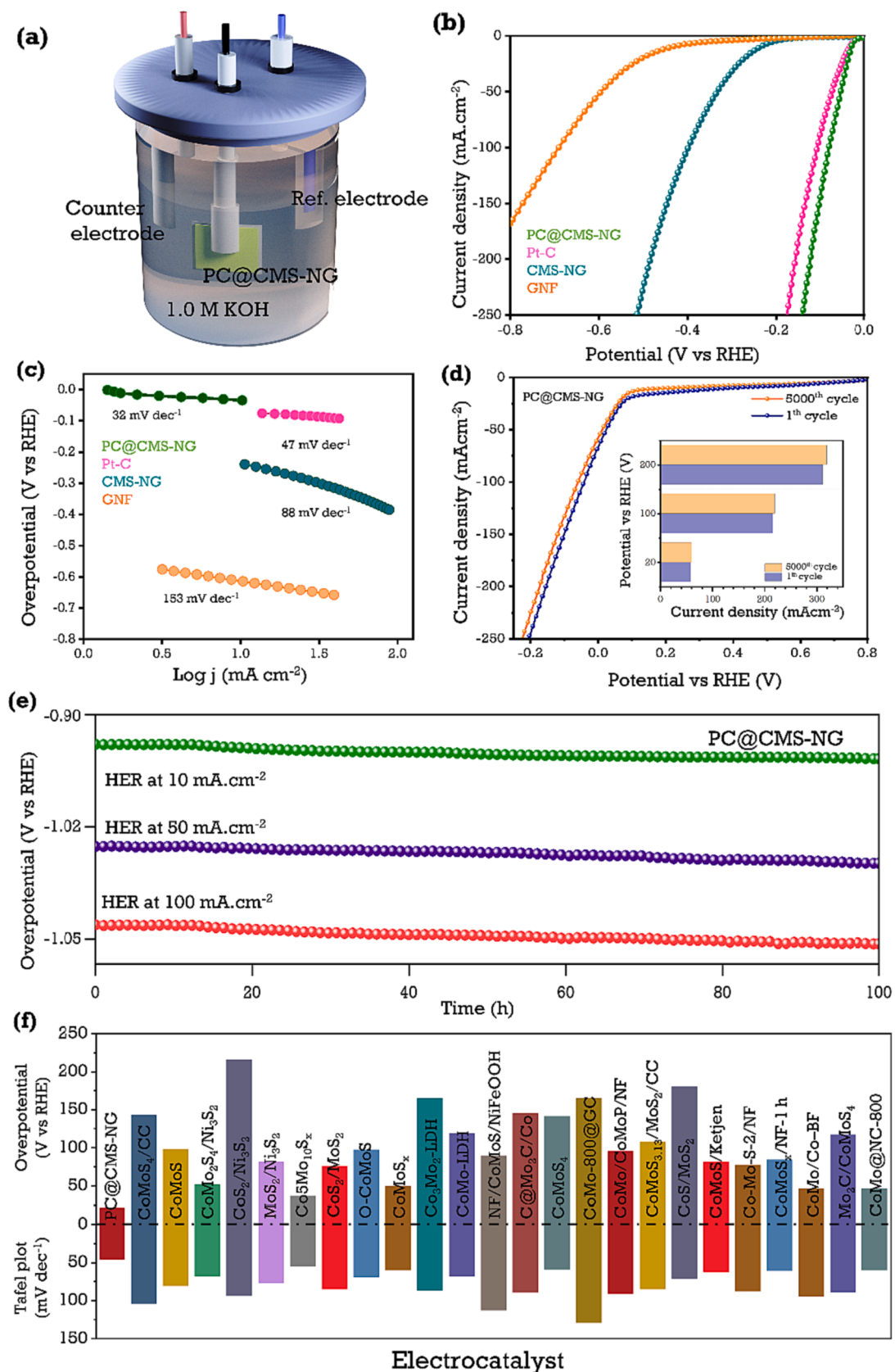


**Fig. 4.** Electrochemical HER performances: (a) Schematic illustration of three electrode cells consisting of PC@CMS-NG as a working electrode. (b) iR-corrected HER polarization curves, (c) respective Tafel slopes of PC@CMS-NG, CMS-NG, GNF, and Pt-C in 1.0 M KOH solution. (d) Cyclic stability responses of PC@CMS-NG, (e) long-term stability tests of PC@CMS-NG at 10, 50, and 100  $\text{mA cm}^{-2}$ , and (f) HER performance comparison chart of recently reported materials with PC@CMS-NG in 1.0 M KOH electrolyte solution.

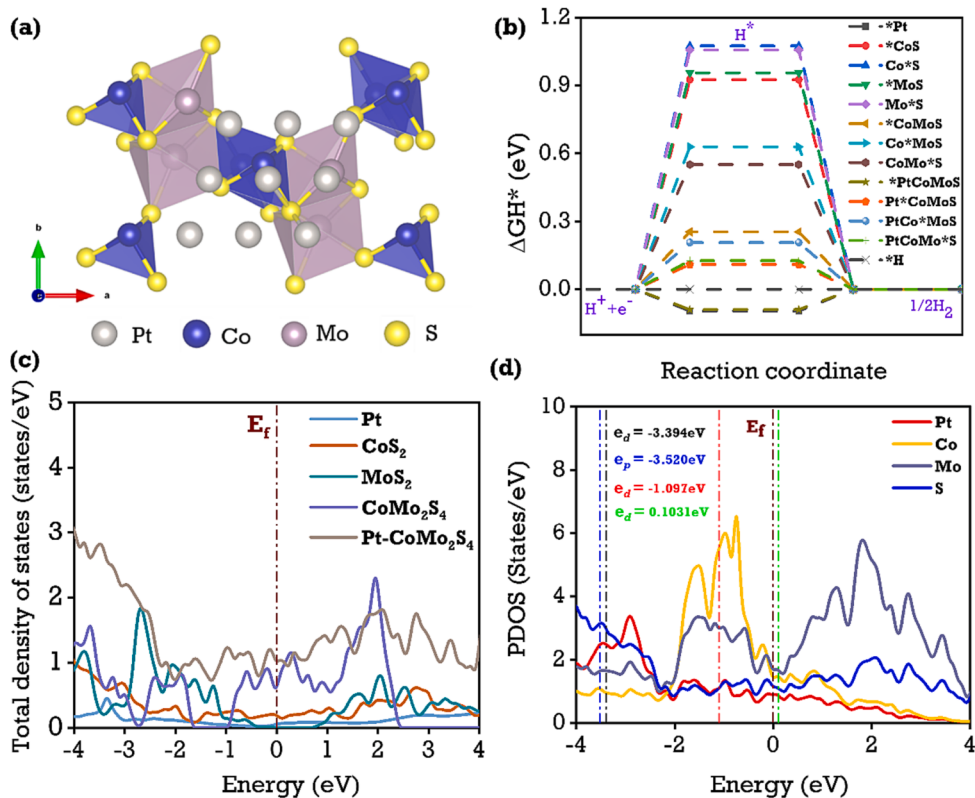


**Fig. 5.** Theoretical HER performances: (a) proposed Pt@CoMo<sub>2</sub>S<sub>4</sub> cell structure, (b) HER adsorption energy calculation profiles of Pt@CoMo<sub>2</sub>S<sub>4</sub>, Pt, CoS, MoS, and CoMoS types, (c) DOS (density of states) of Pt@CoMo<sub>2</sub>S<sub>4</sub>, CoS<sub>2</sub>, MoS<sub>2</sub>, CoMo<sub>2</sub>S<sub>4</sub>, Pt, and (d) PDOS (projected density of states) of Pt, Co, Mo, and S.

conducted. Fig. 5(a-b) shows that the Pt-CoMo<sub>2</sub>S<sub>4</sub>, exhibited a dominance of the electronic states close to the Fermi level, superior to CoMo<sub>2</sub>S<sub>4</sub>, MoS<sub>2</sub>, and Pt. Moreover, the projected density of states (PDOS) analysis depicts the optimal catalyst has highly contributed with d-orbitals, thereby the “Co-3d” located closer to Fermi level at -1.098 eV, indicating this catalyst demonstrates a higher possibility of binding and facilitating electron transfer, thereby enhancing conductivity through stronger interactions between metal atoms and intermediates [46,47]. These DFT results agree with the XPS and EXAFAS measurements. Hydrogen adsorption-free energy ( $\Delta G_{H^*}$ ) is a crucial parameter in theoretical predictions for the HER activity of a material. It is well known that an effective electrocatalyst will have a good  $\Delta G_{H^*}$  values which is close to 0 eV, this suggests suitable HER activity and a low reaction barrier. As a result, Pt@CoMo<sub>2</sub>S<sub>4</sub> is more advantageous regarding Gibbs free energy at the active site of “Pt” where  $\Delta G_{H^*} = -0.089$  eV. At the same time, our catalyst is more effective than commercial Pt = -0.096 eV, as shown in Fig. 5(c-d). Additionally, the active sites of Pt-CoMoS are Co = 0.110 eV, Mo = 0.207 eV, and S = 0.127 eV, which are smaller than comparable co-catalysts and their active sites. Each catalyst value was recorded in Table S4. Compared to the CoMo<sub>2</sub>S<sub>4</sub>, MoS<sub>2</sub>, and CoS<sub>2</sub> surfaces, the Pt-CoMo<sub>2</sub>S<sub>4</sub> adsorption-free energy of DFT calculations and DOS demonstrated improved catalytic performance.

### 3.4. Overall water electrolysis/seawater electrolysis

To test the practical application of the typically prepared PC@CMS-NG electrocatalysts, a homemade two-electrode system was constructed using PC@CMS-NG as the cathodic electrode and commercial IrO<sub>2</sub> as an anodic electrode. Seawater employed as an electrolyte for hydrogen production has become a hot topic [48]. In this study, we tested the alkaline water and 1.0 M KOH-added seawater electrolyte used in overall electrolysis systems. In Fig. 6a, the PC@CMS-NG||IrO<sub>2</sub>-employed cell required a voltage of 1.51 V to reach the benchmark current density

of 10 mA cm<sup>-2</sup>, which is much smaller than the cell voltage of a Pt-C||IrO<sub>2</sub> couple (1.52 V) in alkaline electrolyte. Further, we studied the electrochemical performances of PC@CMS-NG nanohybrids at large current densities in an alkaline media. At the current densities of 50, 200, and 400 mA cm<sup>-2</sup>, overall cell with PC@CMS-NG nanohybrids required potentials of 1.58, 1.71, and 1.81 V, respectively, which are much lower than that of the Pt-C||IrO<sub>2</sub> couple shown in inset Fig. 6a. Additionally, we inserted a real-time comparison study of recently published materials of overall cells with PC@CMS-NG||IrO<sub>2</sub> couples in alkaline media. Similarly, we conducted overall cell LSV tests for PC@CMS-NG||IrO<sub>2</sub> in 1.0 M KOH + seawater electrolyte, which shows an overpotential of 1.54 V at a current density of 10 mA cm<sup>-2</sup> and 1.59, 1.68, and 1.78 V at 50, 200, and 400 mA cm<sup>-2</sup> current densities in Fig. 6b. In Fig. 6c, as shown, a PC@CMS-NG||IrO<sub>2</sub> couple can compete with recent trends in industrial-level hydrogen production applications. Fig. 6d shows the proposed seawater electrolyte-employed water electrolysis cell setup with PC@CMS-NG||IrO<sub>2</sub> electrodes. Generally, seawater-based electrolysis is severely suppressed by chlorine and hypochlorite formation due to the chlorine evolution reaction (CLER) [49]. Theoretically, the CLER is derived from the primary chlorination reaction at  $E^\circ = 1.72$  V<sub>RHE</sub>, which occurs around the minimum overpotential of 495 mV. The calculated potential of PC@CMS-NG||IrO<sub>2</sub> suggests that it has the ability to operate at higher current density when used in seawater-based electrolysis applications. Further, we compared recently communicated seawater electrolysis-based studies with PC@CMS-NG||IrO<sub>2</sub> in Fig. 6e. Fig. 6f shows the more extended durability evaluations of PC@CMS-NG||IrO<sub>2</sub> couples in alkaline water and 1.0 M KOH + seawater electrolyte for 40 h at 50 mA cm<sup>-2</sup>. This figure shows that the stability capability of PC@CMS-NG electrocatalysts in which the minimum potential window gap for alkaline water and 1.0 M KOH + seawater electrolytes is around 0.19 V. Comparison studies of PC@CMS-NG overall water electrolysis performances with recently published electrocatalyst materials are listed Table S5 and Table S6. We also

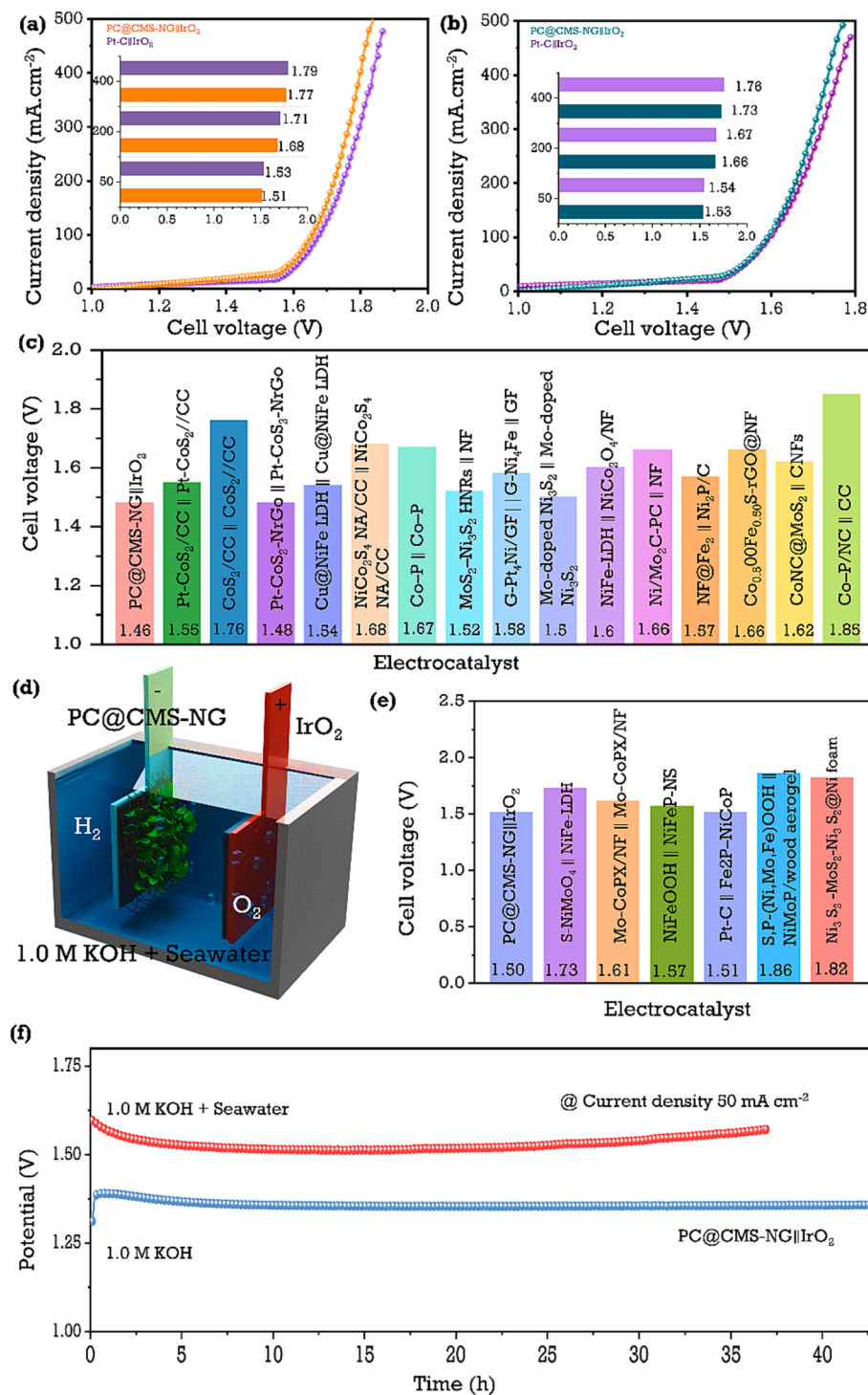


**Fig. 6.** Overall and seawater electrolysis: (a and b) Overall cell polarization curves of PC@CMS-NG||IrO<sub>2</sub> and Pt-C||IrO<sub>2</sub> in 1.0 M KOH and 1.0 M KOH + seawater electrolytes, respectively, (c) overall cell comparison chart of recently reported materials with Pt-C@CoMoS-NGNF in 1.0 M KOH, (d) the proposed seawater electrolysis system equipped with PC@CMS-NG||IrO<sub>2</sub>, (e) Overall cell comparison chart of recently reported materials with PC@CMS-NG in 1.0 M KOH + seawater electrolytes, (f) long-term durability tests of PC@CMS-NG||IrO<sub>2</sub> at 50 mA cm<sup>-2</sup> in 1.0 M KOH and 1.0 M KOH + seawater electrolytes, respectively.

measured the overall cell Faradaic efficiency (FE) with alkaline and alkaline seawater for PC@CMS-NG||IrO<sub>2</sub> couples. We measured the respective gases in separate measuring cylinders with respect to time. FE values were approximately 98 and 94% for the evolved H<sub>2</sub> and O<sub>2</sub> in an alkaline medium 97 and 94% for the evolved H<sub>2</sub> and O<sub>2</sub> in an alkaline seawater medium, respectively, as shown in Fig. S18. From the electrochemical and structural morphology studies above, PC@CMS-NG nanohybrids can be endorsed for their superior catalytic properties, outstanding HER activity, and high stability. First, the hierarchical CoMo<sub>2</sub>S<sub>4</sub> growth on GNF carbon skeletons offers numerous active sites for H<sub>ad</sub>, and an additional Pt-C core–shell development process increases

the porous nature of the electrochemically active surface areas. This construction of PC@CMS-NG nanohybrids was beneficial in terms of HER activity. Therefore, PC@CMS-NG nanohybrids provide remarkable HER electrochemical performance in alkaline and alkaline seawater electrolytes.

#### 4. Conclusion

In summary, we successfully fabricated carbon-encapsulated Pt core–shell supported CoMo<sub>2</sub>S<sub>4</sub>-NGNF for efficient, active, and long-lasting HER electrocatalyst in alkaline and alkaline seawater

electrolytes. The interior PC@CMS-NG has numerous active Pt-C core shells with hierarchical CoMo<sub>2</sub>S<sub>4</sub> surfaces, which ensures effective charge transfer capability with enhanced active surface areas. This CoMo<sub>2</sub>S<sub>4</sub> worked as active metal catalyst and was helpful for corrosion resistance to CLER reactions in the seawater electrolysis approach. At the same time, the typically prepared PC@CMS-NG with significant porosity was favorable for electrolyte diffusion and gas evolution reactions. Hence, this PC@CMS-NG HER electrocatalyst requires only 27, 79, 119, and 140 mV to obtain respective current densities of 10, 100, 200 mA cm<sup>-2</sup>, and 250 mA cm<sup>-2</sup>. Pairing with IrO<sub>2</sub> catalysts to set up the overall cell requires only 1.51, 1.64, 1.72, and 1.74 V to reach the high current densities of 10, 100, 200, and 250 mA cm<sup>-2</sup>, respectively. Eventually, the overall electrolysis cell showed remarkable durability at 10 mA cm<sup>-2</sup> up to 43 h duration. These findings suggest new methods for designing and fabricating Pt-containing robust and effective electrocatalysts for scalable hydrogen production through blending and natural electrolytes.

### Declaration of Competing Interest

The authors declare that they have no known competing financial interests or personal relationships that could have appeared to influence the work reported in this paper.

### Data availability

The data that has been used is confidential.

### Acknowledgments

This research was supported by the GEONJI Research support program. This research was supported by Basic Science Research through the National Research Foundation of Korea (NRF) funded by the Ministry of Education (NRF-2021R1I1A1A01050905). This work was supported by grants from the Medical Research Center Program (NRF-2017R1A5A2015061) through the National Research Foundation (NRF), which is funded by the Korean government (MSIP).

### Appendix A. Supplementary data

Supplementary data to this article can be found online at <https://doi.org/10.1016/j.cej.2023.145348>.

### References

- [1] Ü. Ağbulut, G. Yıldız, H. Bakır, F. Polat, Y. Biçen, A. Ergün, A.E. Gürel, Current practices, potentials, challenges, future opportunities, environmental and economic assumptions for Turkey's clean and sustainable energy policy: a comprehensive assessment, *Sustainable Energy Technologies and Assessments* 55 (2023) 103019.
- [2] R. Hren, A. Vučjanović, Y. Van Fan, J.J. Klemeš, D. Krajnc, L. Čúcek, Hydrogen production, storage and transport for renewable energy and chemicals: An environmental footprint assessment, *Renew. Sustain. Energy Rev.* 173 (2023), 113113.
- [3] H. Jie, I. Khan, M. Alharthi, M.W. Zafar, A. Saeed, Sustainable energy policy, socio-economic development, and ecological footprint: the economic significance of natural resources, population growth, and industrial development, in: *Utilities Policy*, 81, 2023.
- [4] A. Razzaq, A. Sharif, S. Afshan, C.J. Li, Do climate technologies and recycling asymmetrically mitigate consumption-based carbon emissions in the United States? New insights from quantile ardl, *Technological Forecasting and Social Change* 186 (2023), 122138.
- [5] J.R. Zhu, Y. Jin, W. Zhu, D.-K. Lee, N. Bohlooli, Multi-objective planning of microgrid system considering renewable energy and hydrogen storage systems with demand response, *Int. J. of Hydrogen Energy* 48 (41) (2023) 15626–15645.
- [6] A.G. Olabi, M.A. Abdelkareem, M. Al-murisi, N. Shehata, A.H. Alami, A. Radwan, T. Wilberforce, K.-J. Chae, E.T. Sayed, Recent progress in green ammonia: production, applications, assessment; barriers, and its role in achieving the sustainable development goals, *Energy Conversion and Management* 277 (2023) 116594.
- [7] N.S. Gultom, T.-S. Chen, M.Z. Silitonga, D.-H. Kuo, Overall water splitting realized by overall sputtering thin-film technology for a bifunctional monolithic electrode: a green technology for green hydrogen, *Applied Catalysis B: Environmental* 322 (2023), 122103.
- [8] Z. Xiao, Y. Qian, T. Tan, H. Lu, C. Liu, B. Wang, Q. Zhang, M.T. Sarwar, R. Gao, A. Tang, H. Yang, Energy-saving hydrogen production by water splitting coupling urea decomposition and oxidation reactions, *Journal of Materials Chemistry A* 11 (1) (2022) 259–267.
- [9] Z. Li, X. Zhang, Z. Zhang, P. Chen, Y. Zhang, X. Dong, Dual-metal hydroxide@oxide heterojunction catalyst constructed via corrosion engineering for large-current oxygen evolution reaction, *Appl. Catal., B Environmental* 325 (2023), 122311.
- [10] S. Sanati, A. Morsali, H. García, Efficient bifunctional hydrogen and oxygen evolution reaction electrocatalyst based on the NU-1000/CuCo<sub>2</sub>S<sub>4</sub> heterojunction, *Int. J. of Hydrogen Energy* 48 (39) (2023) 14749–14762.
- [11] Y.-X. Yeh, C.-C. Cheng, P.-S. Jhu, S.-H. Lin, P.-W. Chen, S.-Y. Lu, Core-shell FTO@Co<sub>3</sub>O<sub>4</sub> nanoparticles as active and stable anode catalysts for acidic oxygen evolution reaction and proton exchange membrane water electrolysis, *Journal of Materials chemistry a* 11 (7) (2023) 3399–3407.
- [12] A.V. Vorontsov, P.G. Smirniotis, Advancements in hydrogen energy research with the assistance of computational chemistry, *Int. J. of Hydrogen Energy* 48 (40) (2023) 14978–14999.
- [13] J. Liu, Z. Wang, L. Kou, Y. Gu, Mechanism exploration and catalyst design for hydrogen evolution reaction accelerated by density functional theory simulations, *ACS Sustainable Chemistry & Engineering* 11 (2) (2023) 467–481.
- [14] X. Jiang, W. Li, Y. Liu, L. Zhao, Z. Chen, L. Zhang, Y. Zhang, S. Yun, Electrocatalytic oxidation of 5-hydroxymethylfurfural for sustainable 2,5-furandicarboxylic acid production—from mechanism to catalysts design, *Susmat* 3 (1) (2023) 21–43.
- [15] B. Zhang, G. An, J. Chen, H. Guo, L. Wang, Surface state engineering of carbon dot/carbon nanotube heterojunctions for boosting oxygen reduction performance, *Journal of Colloid and Interface Science* 637 (2023) 173–181.
- [16] A.H. Al-naggar, N.M. Shinde, J.-S. Kim, R.S. Mane, Water splitting performance of metal and non-metal-doped transition metal oxide electrocatalysts, *Coord. Chem. Rev.* 474 (2023), 214864.
- [17] D. Khalafallah, A.A. Farghaly, C. Ouyang, W. Huang, Z. Hong, Atomically dispersed pt single sites and nanoengineered structural defects enable a high electrocatalytic activity and durability for hydrogen evolution reaction and overall urea electrolysis, *Journal of Power Sources* 558 (2023), 232563.
- [18] K. Bhunia, M. Chandra, S. Kumar Sharma, D. Pradhan, S.-J. Kim, A critical review on transition metal phosphide based catalyst for electrochemical hydrogen evolution reaction: gibbs free energy, composition, stability, and true identity of active site, *Coord. Chem. Rev.* 478 (2023), 214956.
- [19] F. Almomani, A. Al-rababah, M. Tawalbeh, A. Al-othman, A comprehensive review of hydrogen generation by water splitting using 2d nanomaterials: photo vs electrocatalysis, *Fuel* 332 (2023), 125905.
- [20] L. Wang, L.i. Song, Z. Yang, Y.-M. Chang, F. Hu, L. Li, L. Li, H.-Y. Chen, S. Peng, Electronic modulation of metal-organic frameworks by interfacial bridging for efficient ph-universal hydrogen evolution, *Adv. Funct. Mater.* 33 (1) (2023) 2210322.
- [21] R. Yuan, Y. Wei, B. Musikavanh, M. Tang, Z. Xue, A. Wang, J. Zhang, X. Qiu, L. Zhao, Asymmetric cobalt porphyrins for oxygen reduction reactions: boosted catalytic activity by the use of triphenylamine, *Mol. Catal.* 534 (2023), 112805.
- [22] T. Zhao, X. Huang, R. Cui, W. Han, G. Zhang, Z. Tang, Design of confined catalysts and applications in environmental catalysis: original perspectives and further prospects, *Journal of Cleaner Production* 390 (2023), 136125.
- [23] S. Ma, W. Han, W. Han, F. Dong, Z. Tang, Recent advances and future perspectives in mof-derived single-atom catalysts and their application: a review, *Journal of Materials Chemistry A* 11 (7) (2023) 3315–3363.
- [24] S. Dutta, P. Kumar, S. Yadav, R.D. Sharma, P. Shivaprasad, K.S. Vimaleswaran, A. Srivastava, R.K. Sharma, Accelerating innovations in ch activation/functionalization through intricately designed magnetic nanomaterials: from genesis to applicability in liquid/regio/photo catalysis, *Catal. Commun.* 175 (2023), 106615.
- [25] I. Xuan, Y. Wang, J. Lan, K. Tao, C. Zhou, D. Mei, Development of cathode ordered membrane electrode assembly based on TiO<sub>2</sub> nanowire array and ultrasonic spraying, *Energy* 264 (2023), 126243.
- [26] T. Ali, H. Wang, W. Iqbal, T. Bashir, R. Shah, Y. Hu, H. Hu, electro-synthesis of organic compounds with heterogeneous catalysis, *Adv. Sci. 10 (1)* (2023) 2205077.
- [27] H. Su, J. Jiang, S. Song, B. An, N. Li, Y. Gao, L. Ge, Recent progress on design and applications of transition metal chalcogenide-associated electrocatalysts for the overall water splitting, *Journal of Catalysis* 44 (2023) 7–49.
- [28] Y. Zheng, L. Wang, J. Pang, K. Sun, J. Hou, G. Wang, W. Guo, L. Chen, Ni<sub>3</sub>S<sub>2</sub>/Co<sub>9</sub>S<sub>8</sub> embedded poor crystallinity NiCo layered double hydroxides hierarchical nanostructures for efficient overall water splitting, *Journal of Colloid and Interface Science* 637 (2023) 85–93.
- [29] S. Venkateshwaran, A. Ajith, V. Duraisamy, A. Krishnan, S.M. Senthil Kumar, Tailoring of 1T Phase-Domain MoS<sub>2</sub> Active Sites with Bridging S 22-/Apical S<sub>2</sub>-Phase-Selective Precursor Modulation for Enriched HER Kinetics, *Inorg. Chem.* 62 (2) (2023) 841–852.
- [30] R. Santhosh Kumar, S.C. Karthikeyan, S. Ramakrishnan, S. Vijayapradeep, A. R. Kim, J.-S. Kim, D.J. Yoo, Anion dependency of spinel type cobalt catalysts for efficient overall water splitting in an acid medium, *Chem. Eng. J.* 451 (2023), 138471.
- [31] E.C. Agwamba, H. Louis, B.B. Isang, G.J. Ogunwale, O.J. Ikenyirimba, S. Adeyinka, Pristine fullerene (C<sub>60</sub>) metals (Mo, Fe, Au) engineered nanostructured materials as an efficient electro-catalyst for hydrogen evolution reaction (HER): a density functional theory (DFT) study, *Mater. Chem. and Physics* 297 (2023), 127374.

- [32] W. Zhang, J. Chang, Y. Yang, Strong precious metal–metal oxide interaction for oxygen reduction reaction: a strategy for efficient catalyst design, *Susmat* 3 (1) (2023) 2–20.
- [33] J. Wu, X. Qin, Y.u. Xia, Y. Zhang, B. Zhang, Y. Du, H.-L. Wang, S. Li, P. Xu, Surface oxidation protection strategy of CoS<sub>2</sub> by V<sub>2</sub>O<sub>5</sub> for electrocatalytic hydrogen evolution reaction, *Nanoscale Horiz.* 8 (3) (2023) 338–345.
- [34] T. Pu, W. Zhang, M. Zhu, Engineering heterogeneous catalysis with strong metal–support interactions: characterization, theory and manipulation, *Angew. Chem. Int. Ed.* 62 (4) (2023) e202212278.
- [35] X. Mao, Z. Qin, S. Ge, C. Rong, B. Zhang, F. Xuan, Strain engineering of electrocatalysts for hydrogen evolution reaction, *Mater. Horiz.* 10 (2) (2023) 340–360.
- [36] M. Zhang, H. Li, J. Chen, F.-X. Ma, L. Zhen, Z. Wen, C.-Y. Xu, High-loading co single atoms and clusters active sites toward enhanced electrocatalysis of oxygen reduction reaction for high-performance Zn-air battery, *Adv. Funct. Mater.* 33 (4) (2023) 2209726.
- [37] L.A. Zavala, K. Kumar, V. Martin, F. Maillard, F. Maugé, X. Portier, L. Oliviero, L. Dubau, Direct Evidence of the Role of Co or Pt, Co Single-Atom Promoters on the Performance of MoS<sub>2</sub> Nanoclusters for the Hydrogen Evolution Reaction, *ACS Catal.* 13 (2) (2023) 1221–1229.
- [38] Q. Xie, X. Wang, W. Chen, C. Lei, B. Huang, Engineering active heterojunction architecture with oxygenated-co, mo bimetallic sulfide heteronanosheet and graphene oxide for peroxymonosulfate activation, *Journal of Hazardous Materials* 448 (2023), 130852.
- [39] S. Chen, Z. Cao, F. Gao, H. An, H. Wang, Z. Zhou, L. Mi, Y. Li, 1T-MoS<sub>2</sub>/Co<sub>3</sub>S<sub>4</sub>/Ni<sub>3</sub>S<sub>2</sub> nanoarrays with abundant interfaces and defects for overall water splitting, *Colloids and Surfaces a: Physicochemical and Engineering Aspects* 661 (2023), 130930.
- [40] A.K. Kunhiraman, A. Prabhu, S.A. Kareem, Chalcogenic heterostructure supported on carbon nanostructure for electrochemical water dissociation, *Int. J. Hydrogen Energy* (2022).
- [41] H. Venkatesvaran, S. Balu, B.-S. Tsai, T.C.-K. Yang, Construction of z-scheme heterojunction based on biobr-nanoflakes embedded sulfonic-acid-functionalized g-c<sub>3</sub>n<sub>4</sub> for enhanced photocatalytic removal of hazardous pollutants in aqueous media, *Journal of the Taiwan Institute of Chemical Engineers* 142 (2023), 104637.
- [42] S. Mangel, L. Houben, M. Bar Sadan, The effect of atomic disorder at the core–shell interface on stacking fault formation in hybrid nanoparticles, *Nanoscale* 8 (40) (2016) 17568–17572.
- [43] H. Xu, Y. Jiao, S. Li, H. Meng, J. Wu, X. Shi, Z. Du, R. Wang, G. Tian, Ultrathin-layered mos<sub>2</sub> hollow nanospheres decorating ni<sub>3</sub>s<sub>2</sub> nanowires as high effective self-supporting electrode for hydrogen evolution reaction, *Int. J. Hydrogen Energy* 45 (24) (2020) 13149–13162.
- [44] X. Zheng, J. Xu, K. Yan, H. Wang, Z. Wang, S. Yang, Space-confined growth of mos<sub>2</sub> nanosheets within graphite: the layered hybrid of mos<sub>2</sub> and graphene as an active catalyst for hydrogen evolution reaction, *Chemistry of Materials* 26 (7) (2014) 2344–2353.
- [45] N. Nwaji, H. Kang, M. Goddati, L.T. Tufa, J. Gwak, A. Sharan, N. Singh, J. Lee, Sulphur vacancy induced Co<sub>3</sub>S<sub>4</sub>@CoMo<sub>2</sub>S<sub>4</sub> nanocomposites as a functional electrode for high performance supercapacitors, *Journal of Materials Chemistry A* 11 (7) (2023) 3640–3652.
- [46] Y.u. Gu, S. Chen, J. Ren, Y.A. Jia, C. Chen, S. Komarneni, D. Yang, X. Yao, Electronic Structure Tuning in Ni<sub>3</sub>FeN/r-GO Aerogel toward Bifunctional Electrocatalyst for Overall Water Splitting, *ACS Nano* 12 (1) (2018) 245–253.
- [47] Q.i. Ouyang, S. Cheng, C. Yang, Z. Lei, Vertically grown p–n heterojunction FeCoNi LDH/CuO arrays with modulated interfacial charges to facilitate the electrocatalytic oxygen evolution reaction, *Journal of Materials Chemistry A* 10 (22) (2022) 11938–11947.
- [48] K. Guo, D. Xu, I. Xu, Y. Li, Y. Tang, Noble metal nanodendrites: growth mechanisms, synthesis strategies and applications, *Mater. Horiz.* 10 (4) (2023) 1234–1263.
- [49] K. Poonia, S. Patial, P. Raizada, T. Ahamad, A.A. Parwaz Khan, Q. Van Le, V.-H. Nguyen, C.M. Hussain, P. Singh, Recent advances in Metal Organic Framework (MOF)-based hierarchical composites for water treatment by adsorptive photocatalysis: a review, *Environ. Res.* 222 (2023), 115349.